Intrinsic photoanode band engineering: enhanced solar water splitting efficiency mediated by surface segregation in Ti-doped hematite nanorods

Stefan Stanescu[a]*, Théo Alun[b], Yannick J. Dappe[b], Dris Ihiawakrim[c], Ovidiu Ersen[c], and Dana Stanescu[b]*

[a] Synchrotron SOLEIL, L'Orme des Merisiers, Départementale 128, 91190 Saint-Aubin, France

E-mail: stefan.stanescu@synchrotron-soleil.fr

[b] SPEC, CEA, CNRS, Université Paris-Saclay, CEA Saclay 91191 Gif-sur-Yvette Cedex, France

E-mail: dana.stanescu@cea.fr

[c] Institut de Physique et Chimie des Matériaux de Strasbourg (IPCMS), CNRS UMR 7504, 23 rue du Loess, BP43, 67034 Strasbourg, France

Abstract

Band engineering is thoroughly employed nowadays targeting technologically scalable photoanodes for solar water splitting applications. Most often complex and costly recipes are necessary, for average performances. Here we report very simple photoanode growth and thermal annealing, with effective band engineering results. Strongly enhanced photocurrent, of more than 200 %, is measured for Ti-doped hematite nanorods grown from aqueous solutions and annealed under Nitrogen atmosphere, compared to air annealed ones. Oxidized surface states and increased density of charge carriers are found responsible for the enhanced photoelectrochemical activity, as shown by electrochemical impedance spectroscopy and synchrotron X-rays spectromicroscopies. They are found related to oxygen vacancies, acting as n-dopants, and the formation of pseudo-brookite clusters by surface Ti segregation. Spectro-ptychography is used for the first time at Ti L_3 absorption edge to isolate Ti chemical coordination arising from pseudo-brookite clusters contribution. Correlated with electron microscopy investigation and Density Functional Theory (DFT) calculations, our data unambiguously prove the origin of the enhanced photoelectrochemical activity of N_2-annealed Ti-doped hematite nanorods. Finally, we present here a handy and cheap surface engineering method beyond the known oxygen vacancy doping, allowing a net gain in the photoelectrochemical activity for the hematite-based photoanodes.

1. Introduction

Hydrogen production by solar water splitting (SWS) using abundant and eco-friendly photoelectrode materials is very appealing nowadays. The overall efficiency of SWS reaction is directly related to the photoelectrochemical (PEC) activity including both oxidation and reduction reactions that occur at the interface between photoelectrodes and the aqueous electrolyte. Hematite is the archetype semiconducting material used as photoanode, presenting a band gap of 2.15 eV perfectly matching the solar spectrum for optimized absorption and thus for direct SWS applications. However, pristine hematite presents low SWS efficiency because of the reduced hole mean free path (~ 2 – 4 nm) and poor surface kinetics related to a complex oxygen evolution reaction (OER) [1–5]. It was largely demonstrated that surface kinetics during SWS can be tuned by controlling surface states nature using various band engineering approaches: doping [6–8], hetero- and nano-structuring [9–13], annealing [14,15], catalyst film coating [16–21], etc. In particular the synergic effect between Ti-doping and induced oxygen vacancies through thermal treatments during or post growth under oxygen depleted atmosphere has shown its efficiency [22–26]. Various mechanisms were suggested to contribute to the enhancement of PEC activity. Zhao et al. [23] have shown that by annealing pristine and Ti-doped hematite photoanodes in Nitrogen gas at 600°C the photocurrent is increased by 200 % and 67 % respectively. They assigned this enhancement to oxygen vacancies generated by nitrogen treatment, leading to carrier density increase. Moreover, opposite behaviors were found for the charge transfer processes, comparing pristine hematite and Ti-doped hematite, suggesting increased transfer resistance for the later one. To the contrary, Wang et al. [25] demonstrated strong electrocatalytic surface contribution of the induced oxygen vacancies along to the expected improvement of the bulk conductivity. Such divergences between different reports can be understood taking into account the variety of the employed sample preparation methods, leading to more or less sensitivity to subtle surface effects.

Most of these conclusions are extracted from studies concentrated on PEC macroscopic measurements, nanoscale information being often absent. In this respect, a perfect demonstration is given by Zhang et al. [22], in the case of highly ordered attached Ti-modified hematite mesocrystals. Their thorough study presents strongly enhanced PEC properties promoted by a double contribution: first, the formation of interfacial oxygen vacancies yielding high carrier density, and second, shorter depletion width (< 10 nm) over large regions through formation of rutile TiO_2 at the mesocrystals surface, as determined by high resolution electron microscopy. Indeed, complex hematite-Ti based heterostructures (Fe_2O_3/Fe_2TiO_5 or $Fe_2O_3/FeTiO_3$) were demonstrated to be very effective for PEC activity enhancement [18, 27-30] owing to strongly increased surface charge separation leading thus to increased number of holes injection at the interface with the electrolyte. Most often cumbersome experimental strategies are needed to obtain complex heterostructures, necessitating several growth or treatment cycles and involving various chemical processes.

Here, we report on intrinsic heterostructuring owing to surface segregation of a Ti-rich phase during the annealing under Nitrogen of Ti-doped hematite photoanodes obtained by aqueous growth [14]. For these photoanodes we recorded strong enhancement of the photocurrent and lower flat-band values, compared to air-annealed samples. We correlate macroscopic PEC (photo-voltammetry, EIS – Electrochemical Impedance Spectroscopy) and state-of-the-art synchrotron X-rays spectromicroscopy measurements (S-XPEEM – Shadow X-rays Photoemission Electron Microscopy, STXM – Scanning Transmission X-rays Microscopy, spectro-ptychography), completed by electron microscopy (STEM – Scanning Transmission Electron Microscopy). Our results demonstrate the formation of surface pseudo-brookite clusters yielding partial Ti:Fe_2O_3/Fe_2TiO_5 interface, leading to better charge separation through corresponding surface states. Interestingly, we observe that a very low fraction (estimated to less than 5 %) of the Ti-

doped hematite is covered by pseudo-brookite clusters and thus responsible for the enhanced PEC activity. Efficient charge transport is ensured by enhanced bulk conduction promoted mainly by Ti and, at lesser extent, by oxygen vacancies doping. Finally, we show subtle differences of chemical and electronic structures of hematite nanorods, both in surface and bulk, for Nitrogen and air-annealed photoanodes, guiding further strategies enhancing the SWS efficiency.

2. Results and Discussions

2.1. Fast-sweep and stabilized photo-voltammetry

Photocurrent density, $J_{ph} = J_{ON} - J_{OFF}$, was measured following two protocols as described in a previous work [14]. For that purpose, we measured the current density for light ON (J_{ON}) and respective OFF (J_{OFF}) as a function of the applied potential using a three-electrode electrochemical cell where the photoanode was Nitrogen and air annealed Ti:α-Fe$_2$O$_3$ nanorods films grown by ACG (S1 and S2, respectively – see sections 4.1 and 4.2 for further details). First, voltammetry measurements were performed by varying the voltage between 0.6 and 1.7 V vs. RHE with a sweep rate of 50 mV/s (Figure S1a). Second, photocurrent density was measured as a function of time while keeping the applied voltage constant. Current density is read once stabilized, for nine values of the applied voltage in the interval 0.8 – 1.6 V *vs.* RHE. This protocol allows to measure stabilized photocurrent values as the step height between light OFF and ON values (blue and red dot respectively in Figure S1b). The photocurrent values obtained using the two types of measurements are represented in Figure 1 for both samples, S1 and S2, as a function of the applied potential. First, we evidence an increase of the photocurrent of more than 200 % at 1.23 V *vs.* RHE for S1 compared to S2 sample. Second, we observe that the photocurrent values measured with both protocols are similar. This point was exhaustively discussed in a previous work from our group and related to

low transients that can be observed on the ON – OFF measurements, for annealing temperatures of more than 600 °C [14].
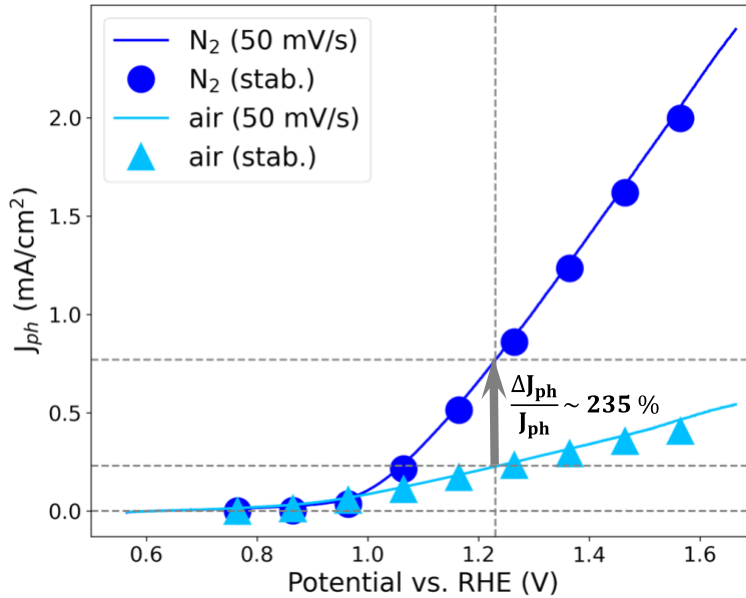

Figure 1. Photocurrent as a function of the applied voltage for S1 (dark blue) and S2 (light blue) samples. Photocurrent values obtained from both protocol measurements are reported: fast-sweep rate (solid lines) and stabilized (symbols). A strong photocurrent increase is observed, of more than 200 %, at 1.23 V *vs.* RHE for S1 with respect to S2. At 1.6 V *vs.* RHE, the photocurrent increases by a factor of 4.

2.2. Flat band potential and carrier density

Electrochemical impedance spectroscopy (EIS) allows characterizing electrical properties of photoanodes, such as the quantification of donors' density (N_d), the estimation of flat band potential (V_{fb}), band bending and charges separation at the interface between the semiconductor and the electrolyte. Nyquist and Mott-Schottky plots are the common "tools" generally used in photoelectrochemistry to find the equivalent circuit that better models the interface in such systems. Mott-Schottky analysis allows determining N_d and V_{fb} values by a simple linear fit of the experimental data represented as $1/C^2$ as a function of the applied potential. This analysis works well for model systems: homogeneous and continuous photoanodes, sufficiently thick. In our case, the photoanodes consist of nanorods, with sizes of few hundreds of nanometers, perpendicular to the FTO substrate. The linear fit from Mott Schottky analysis will not result in accurate absolute

values for N_d and V_{fb} [31, 32] and therefore they should not be compared to other from literature, especially applied on photoanodes presenting different morphology. We use these values here only to compare the electric properties of S1 and S2 samples.

2.2.1. Nyquist plots

Nyquist plots, representing imaginary part, $|Z_{img}|$, as a function of the real part, Z_{re}, were determined for both S1 and S2 photoanodes, for several voltages (V) between 0.7 V and 1.6 V *vs.* RHE, and for different frequencies (f) between 10 Hz and 900 kHz (Figure S2). On each plot, we distinguish two regions: a) high frequency region (from 3 to 900 kHz) corresponding to a semicircle characterizing the internal resistance and RC-like semiconductor impedance, and b) low frequency region (from 10 Hz to 3 kHz) – a slope shape characterizing both the Helmholtz layer formation in the electrolyte near the interface with the photoanode and ion diffusion through the Helmholtz layer. First, we observe reduced impedance values for S1 compared to S2. This result reflects a better overall bulk conduction in the first case due to oxygen vacancies generated during annealing under Nitrogen. Second, the low frequency region slope exhibit two regimes as a function of the applied voltage: i) for V < 1.5 V, charges accumulate in the Helmholtz layer and the capacitive character of the impedance increases (larger $|Z_{img}|$ for similar Z_{re}); ii) for V > 1.5 V, we observe a reduced slope value, originating from ion diffusion through the capacitive layer [14].

2.2.2. Determination of flat band and carrier concentration

Experimental $Z(f)$ spectra were fitted using the equivalent circuit $(R1||Q1) - (R2||Q2) - R3$ shown in Figure S3. $R1$ ($R2$) and $Q1$ ($Q2$) are the resistances (Ri) and the constant-phase-elements (CPE, Qi) associated to the semiconductor photoanode (Helmholtz layer). As detailed in Supporting Information, the values of the capacitance, C, associated with the space charge layer in the semiconducting photoanode in contact with the electrolyte can be calculated with Equation S4, using Qi and N_i parameters resulted from the fit (Figure S4). Mott-Schottky plots, expressing

$1/C^2$ as a function of the voltage obtained at 900 kHz for both photoanodes, are presented in Figure 2. It is important to mention here that Mott-Schottky plots obtained for all frequencies in the interval 10 Hz – 900 kHz are similar. $C(f)$ slopes for multiple potential values are quasi-parallel, particularly for applied potentials between 1.1 and 1.4 V (Figure S5). The simplest model used to fit Mott-Schottky plots supposes a linear variation with the voltage of $1/C^2$. In reality, this linearity is dependent on several parameters such as the semiconductor state (accumulation, depletion or inversion), the presence of surface states, the size of the surface features on the photoanode, electrolyte's pH value, donor levels in the semiconductor, crystallographic structure of the material, etc. [31–35]. For a comparative analysis between samples S1 and S2 we consider that for potentials between 1.1 and 1.4 V (interval materialized by gray region Figure 2), the semiconductor is in depletion state, and the Mott-Schottky plot can be linearly fitted using the simplified formula:

$$\frac{1}{C^2} = \frac{2}{eN_d\varepsilon_0\varepsilon_r S^2}(V - V_{fb} - \frac{K_B T}{e})$$

where C is the capacitance, $e = 1.6 \times 10^{-19}$ C is the electron charge, N_d the carrier concentration, $\varepsilon_0 = 8.85 \times 10^{-12}$ F·m^{-1} and ε_r are the vacuum and relative permittivity, respectively. S is sample surface in contact with the electrolyte ($S = 0.5$ cm^2 in our case), V_{fb} is the flat band, V is the applied voltage, $K_B = 1.38 \times 10^{-23}$ J·K^{-1} is Boltzmann constant and T is the temperature. For hematite, a wide range of relative permittivity values are reported in the literature, depending on the morphology (nanostructures or not), annealing temperature, frequency, etc. [31,36]. This results in a significant difference of the predicted capacitance values. In this work, the value used for the relative permittivity is $\varepsilon_r = 10$, therefore, it will be easy for the reader to recalculate capacitance values if one considers a different value for ε_r. From linear fits in Figure 2, we estimate the flat band values, V_{fb}, of 0.1 V and 0.8 V and carrier concentrations, N_d, of 4.2×10^{21} and 5.4×10^{20} for S1 and S2, respectively. We recall that these values are obtained using a simple linear fit analysis

without any consideration about nanorods dimensions (width, length) or density (in number of nanorods / cm^2). However, their relative variation is employed here for comparative reasons only of the electric properties of S1 and S2 samples.
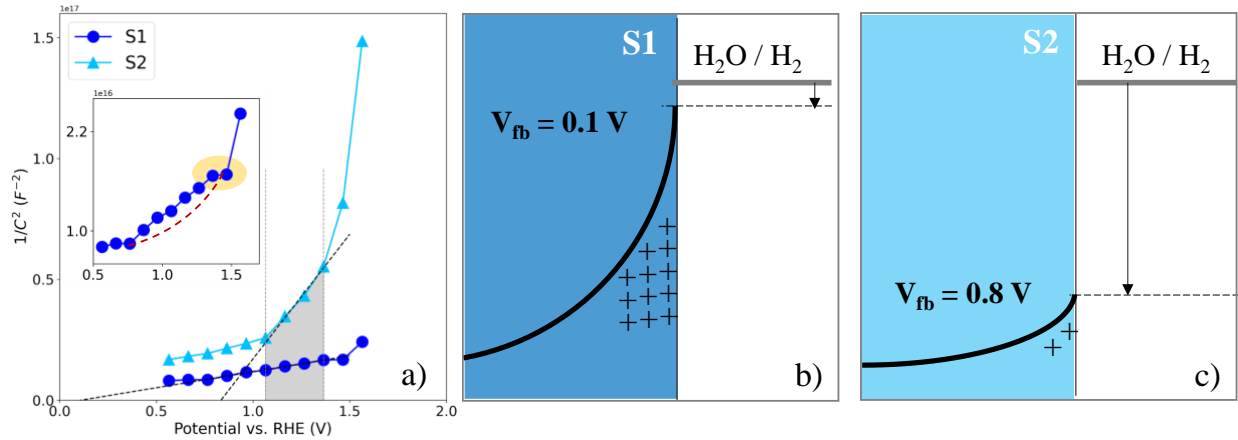

Figure 2. Mott-Schottky analysis for S1 (●) and S2 (Δ) samples (a). Linear fits were performed for potential values between 1.1 V and 1.4 V vs. RHE, emphasized by the grey region. Larger carrier concentrations values ($N_d = 4.2 \times 10^{21}$) are determined for S1 compared to S2 ($N_d = 5.4 \times 10^{20}$). A yellow region in the inset of (a) indicates the kink region, characteristic to the presence of surface states; b) and c) representation of the band bending at the interface with the electrolyte considering the flat band values estimated for S1 (0.1 V) and S2 (0.8 V) samples, respectively.

It is known that surfaces states at the semiconductor/electrolyte interface induce Fermi level pinning, and, in this case, Mott-Schottky characteristic shape presents a plateau (or double kink) where the $C(V)$ is (quasi-)constant [37,38]. In this region, the applied voltage drops within the Helmholtz layer instead the depletion region in the semiconductor [39]. For S1 sample, this flat region can be observed for voltages between 1.4 and 1.5 V (marked region in Figure 2a). To the contrary, nothing is visible for S2 photoanode. As shown in previous studies [14, 40] two kind of surface states may co-exist at the interface between the hematite-based photoanode and the electrolyte, one at higher oxidative energies, lying at the bottom of the conduction band and a second at lower energies. While the first kind is beneficial for the PEC process, the second plays a detrimental role as being inactive from the PEC point of view, driving recombination of charges at the interface. In the present case, we identify beneficial (i.e. with higher oxidative energy) surface

states leading to lower flat band value for the S1 sample, that determines a higher band bending at the interface with the electrolyte (Figure 2b), and, consequently, better charge separation. Furthermore, we find a carrier concentration ten times higher for S1 than for S2, which confirms previous observations related to improved electric conduction. Therefore, we can conclude that there are two mechanisms determining higher photocurrent induced by N_2 atmosphere annealing: i) at surface, due to better charges separation promoted by surface states, and ii) in bulk, by improved electric conductivity due to higher carrier concentration. It is interesting to focus here briefly on the preponderance of each of these mechanisms. First, it is an accepted fact that Ti doping increases the electrical conductivity acting as *n* doping in the hematite semiconductor, increasing thus the measured photocurrent during the PEC process. Figure S6 presents the comparison of two samples, one annealed in air and the other under Nitrogen, containing 30 times less Ti compared to S1 and S2 samples. On one hand, it is important to note that even at this very low Ti content level the photocurrent is increased compared to bare hematite. Upon Nitrogen annealing, there is barely any visible difference between the two cases, the sample annealed under Nitrogen exhibiting only slightly higher photocurrents above 1.3 V vs. RHE. It appears thus that for very low Ti contents, the Nitrogen annealing has marginal effects on the recorded photocurrent. Therefore, the increase we might expect from the additional oxygen vacancies doping, formed upon annealing under Nitrogen, is negligible. Consequently, the strong photocurrent increase we measure for the S1 sample compared to the S2 in mainly due to the first mechanism related to the presence of the surface states promoting enhanced charge separation.

2.3. Surface *vs.* bulk chemical composition and coordination

2.3.1. Shadow S-XPEEM

Here we combine photoemission's surface sensitivity along with S-XPEEM capability to discriminate surface and volume chemical and electronic structure information (for details see

Supporting Information, section III). To this purpose, we measured energy stacks by recording full-field XPEEM images while tuning the X-rays energy across the Ti $L_{2,3}$, O K and Fe $L_{2,3}$ absorption edges, from 450 to 750 eV. Figure 3 shows the results obtained for S1 and S2 samples. The RGB color-coded images (Figure 3a for S2 and 3b for S1, respectively) are derived through singular value decomposition (SVD) method applied to the drift-corrected hyperspectral data using its implementation in the aXis2000 software [41]. Three main spectral contributions were used, each one represented by a dedicated colors in Figure 3: bulk one, from the shadow region (Red), gold-plated Si substrate (Green), and surface contribution (Blue) (see also Figure S7 for further details).
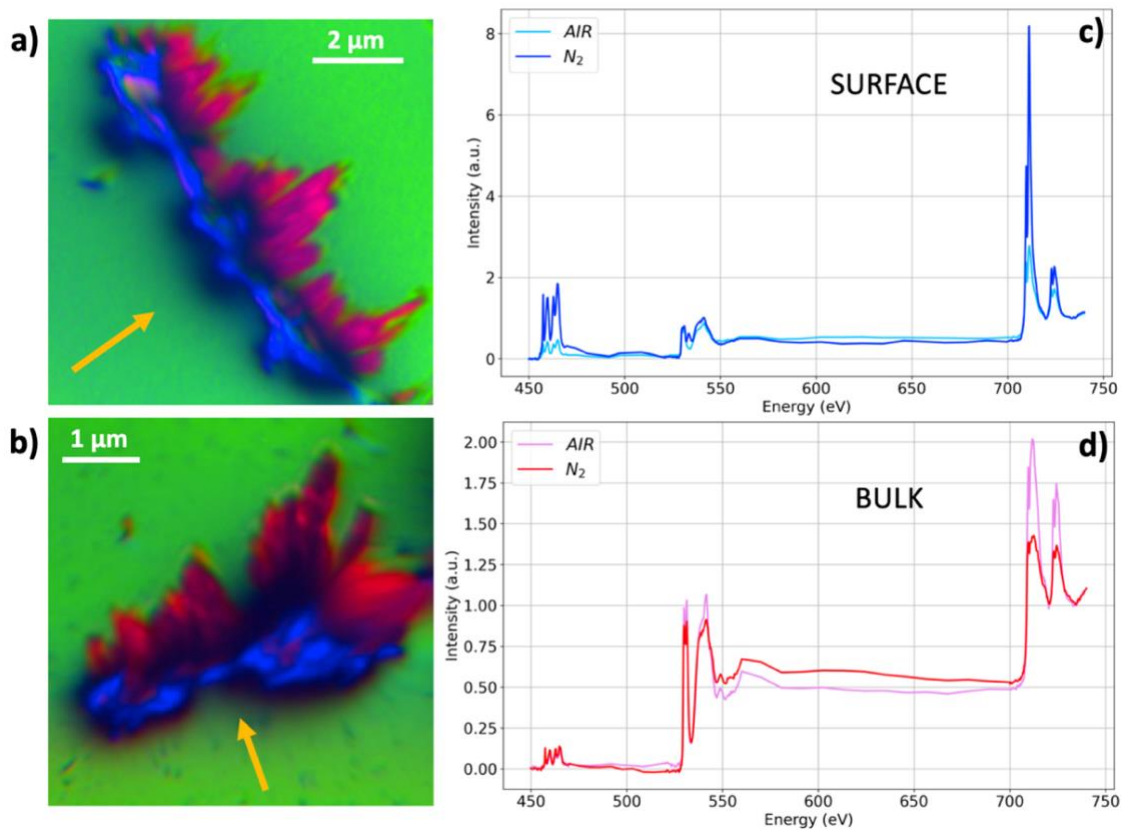

Figure 3. S-XPEEM results from the N_2 (S1) and air annealed (S2) samples; a) and b) RGB color-coded map representations of the 3 regions of interest: **R**ed – bulk (shadow), **G**reen – gold substrate, **B**lue – surface, respectively; the orange arrow indicates the direction of the X-rays beam; the images are kept in the original orientation as given by the electron microscope lens settings for the respective field of views used: 20 μm for S2 samples in a) and 10 μm for S1 sample in b); c) comparison of the surface signals recorded from the corresponding blue regions of both samples: we remark the strong spectral differences at the Ti $L_{2,3}$ (450 – 470 eV) edges and O K edge (520 – 560 eV); d) comparison of the bulk signal recorded from the corresponding red (shadow) regions of both samples: the spectra look very similar, signature of a similar bulk chemical nature of the two samples.

The images shown in Figure 3a and 3b are kept in their raw orientation, as derived from 20 µm and 10 µm fields of views respectively. In the electron microscope column, the image is turned by the specific lens settings for each field of view, while the detection is fixed. Thus, to orient the reader, the direction of the X-ray beam is materialized using the orange arrow. Surface and bulk (shadow) regions can be easily distinguished, marked as blue and red regions, respectively. Considering the 16° incidence of the X-rays, the size of the Ti-doped hematite particles deposited on the gold-plated substrate can be extracted from their shadow size: it spans from 200 to 500 nm. To compare the chemical composition, $i.e.$ the elemental Ti/O/Fe ratio, of the two set of samples, the spectra are normalized in two steps. First, with respect to the incoming X-ray beam intensity, I_0 (Figure S8). Gold-plated substrates were used to fulfil the requirement of a flat spectral response over the useful energy range and used hence as I_0. Since we record two kinds of signals on the sample, $i.e.$ photoemission (surface – blue) and transmission (bulk – red), different I_0 normalization are required. Thus, I/I_0 was used for the surface signal (Figure S8c). The bulk signal is treated likewise a transmission experiment, and optical density can be extracted as $OD = log(I_0/I)$ (Figure S8b). Second, considering that the chemical formula includes Ti, O and Fe only, a straight line is subtracted from the Ti $L_{2,3}$ pre-edge region (450 – 455 eV) bringing this region to zero (removing thus spectral contribution arising from thickness and density), and then the spectra are multiplied such as to be matched over the Fe $L_{2,3}$ post-edge (735 – 740 eV) region. Therefore, the elemental chemical ratio is directly proportional to the edge jumps. Bulk spectra of S1 and S2 samples are very similar, as it can be observed in Figure 3d. Indeed, the edge jumps are almost identical suggesting no difference in the bulk composition between the two samples. Across the Fe $L_{2,3}$ absorption edges, the bulk signal is saturated due to the thickness of the particles ($i.e.$ larger than 200 nm) and the strong X-ray attenuation length that varies between 80 and 120 nm in this

spectral region. No differences can be noted at the resonant energies of Ti, O and Fe. Contrary to bulk spectra, the surface ones show increased edge-jump across the Ti $L_{2,3}$ absorption edge for both samples (Figure S9), signature of surface Ti-segregation, as already shown in the case of air-annealed Ti-doped hematite samples [14]. In addition, the sample annealed in N_2 atmosphere (S1) exhibits higher edge jump (Figure 3c) than the one recorded for the air-annealed (S2) sample, showing thus stronger Ti surface segregation.
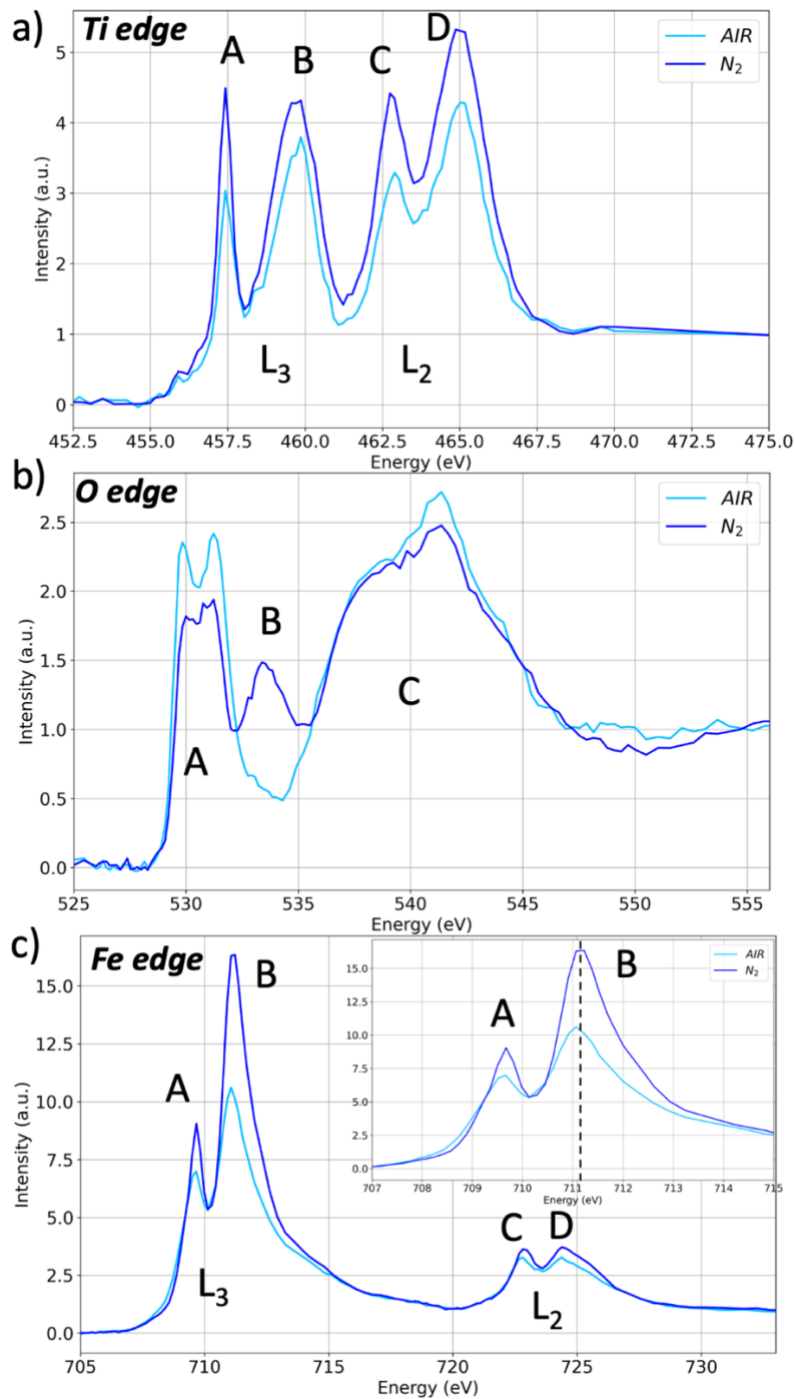
Figure 4. NEXAFS spectra extracted from the surface regions of the S-XPEEM measurements across the Ti $L_{2,3}$ (a), O K (b), and Fe $L_{2,3}$ (c) X-ray absorption edges. Spectra are normalized at each of the absorption edges such as to address only the electronic structure of the probed ion. The major spectral features are labeled as follows: a) Titanium: A – L_3 t_{2g}, B – L_3 e_g, C – L_2 t_{2g}, D – L_2 e_g; b) Oxygen: A – hybridized spectral region showing Fe t_{2g} – e_g and Ti t_{2g} crystal field splitting, B – hybridized Ti e_g, C – hybridized Fe and Ti 4sp bands; c) Iron: same notations as for Titanium in a).

Near-Edge X-ray Absorption Fine Structure (NEXAFS) spectroscopy has the ability to discriminate very fine chemical coordination features. Spectral features in the resonant region of the absorption edges are intimately related to the electronic structure of the probed ion. We present the three spectral regions of interest in Figure 4. With respect to the Figure 3c, where spectra were normalized over the whole energy range (450 – 740 eV), here we apply the same type of normalization, *i.e.* we subtract linear background in the pre-edge region and multiply spectra to match the post-edge, but around each elemental absorption region independently. In this manner we keep only coordination information of the probed ion, and we can thus focus on the electron structure comparison between samples. At the Ti absorption edge, Figure 4a, the S2 sample has typical ilmenite, $FeTiO_3$, spectral shape, with a symmetrical B (Ti L_3 e_g electronic transition) peak [42]. The relative intensities (branching ratio) between the A, B, C and D peaks, are equally characteristic to the Ti^{4+} ion in the ilmenite ($FeTiO_3$) structure (Figure S10). This is expected for an ideal Ti substitution of an octahedrally coordinated Fe^{3+} ion in the hematite (Fe_2O_3), as shown in a previous work [14]. For the S1 sample, the A:B branching ratio changes, the Ti L_3 t_{2g} band having increased intensity compared to S2, while the C:D branching ratio remains constant. This overall spectral shape is very similar to a TiO_2 brookite-like structure [42,43]. Nevertheless, regardless the chemical information detailed above, we cannot consider TiO_2 alone at the surface of S1 samples and it is more reasonable to consider a pseudo-brookite structure, $Fe_{1+x}Ti_{2-x}O_5$, with *x* between 0 and 1. The corresponding crystallographic structures are represented in Figure S10. It is impossible, considering the spectral shape alone, to define a particular value for *x*, since the Ti^{4+} ion has the same octahedral coordination (Ti-O_6) over the entire x range, from 0 to 1. Additional information can be extracted from the NEXAFS Fe spectra in Figure 4c. First, it is interesting to remark that contrary to what one would expect, the S2 sample presents a slight reduction of the Fe^{3+}, the B line being shifted toward lower binding energies by < 0.1 eV with respect to the S1

sample, shown for clarity as inset in Figure 4c. This leads also to a variation of the d-orbital splitting, $t_{2g} - e_g$ (A-B), from 1.48 eV for S1 to 1.41 eV for S2. Distortions of the Fe-O_6 octahedra very close to the hematite nanoparticles surface, that are probed in this case, and the Ti substitution in the hematite structure, may explain such behavior [44]. Since S1 sample presents increased Ti content toward the surface, this distortion is further accentuated. In addition to the structural origin of this behavior, we must consider that during the transformation of hematite into ilmenite through Ti substitution, part of the Fe^{3+} from the hematite structure is replaced by Ti^{4+} through iron reduction to Fe^{2+}, following the charge conservation relation: $2 \cdot Fe^{3+} = Fe^{2+} + Ti^{4+}$. Therefore, for S2, the slight iron reduction agrees with the spectral shape measured at Ti absorption edge (Figure 4a) and related to formation of ilmenite ($FeTiO_3$). Conversely, S1 sample exhibits increased proportion of Fe^{3+}, signature for the formation of the pseudo-brookite phase, $Fe_{1+x}Ti_{2-x}O_5$ with $x = 1$,[45] capable of holding high concentration of Fe^{3+} oxidation state from charge equilibrium criteria, in agreement with the NEXAFS spectra recorded at Ti edge (Figure 4a). Unfortunately, the literature lacks extended reports of pseudo-brookite NEXAFS at the Fe $L_{2,3}$ absorption edge for further comparison. Lv et al. [30] reported recently Fe $L_{2,3}$ NEXAFS recorded in total electron and fluorescence yield modes, for either coated or incorporated Fe_2TiO_5 into hematite, evidencing only Fe^{3+} related to the formation of the pseudo-brookite phase, but without any further developments, as for instance the value of the measured branching ratio in that case. Indeed, a second notable feature that can be extracted from the Fe $L_{2,3}$ NEXAFS, is the variation of A:B branching ratio that has a value of 0.65, for S2, as expected for hematite [44]. To the contrary, S1 exhibits a value of 0.56, equivalent to an iron oxyhydroxide, likewise goethite for instance. First-order influence in the branching ratio arises from the Fe oxidation state. As demonstrated by the Fe L_3-e_g (B) energy shift, the Fe^{3+} is partially reduced in S2. This could explain alone the branching ratio variation

between the two samples. However, we cannot exclude other first-order influences like the ligand field strength (or crystal field strength), that varies from 1.48 to 1.41 eV, as explained above.

The O K-edge NEXAFS (Figure 4b) is of particular interest for oxide materials in general, due to the delocalized character of the O 2p orbitals, responsible hence for their conduction properties [46]. Thus, we probe in this case directly the unoccupied electronic states available in the conduction band. The spectra exhibit two distinct regions, below and above ~535 eV. Below, in the A region, we distinguish spectral features related to electronic transitions from the O 1s to hybridized Fe 3d – O 2p bands, showing the d-orbital splitting, t_{2g} and e_g, likewise the Fe $L_{2,3}$ absorption edge. Above (C region), there are mixed O 2p and hybridized Fe 4sp – O 2p bands. The air-annealed (S2) sample shows typical line shape for surface character of Ti-doped hematite, as already shown [14]: prominent Fe 3d – O 2p hybridization, and the presence of oxidized surface states (OSS) marked by a strong asymmetry in the spectral region labelled with B. At the same energy position, the N_2-annealed (S1) sample displays a peak. In addition, the d-orbital splitting value of S1 is clearly reduced compared to S2, in agreement with the spectra recorded at Fe $L_{2,3}$ edge (Figure 4c). Owing to the Fe_2TiO_5 formation at the surface of the sample, we are obviously probing here a mixture of hematite and titanate character. Before a detailed comparison with data from literature, it is mandatory to note that NEXAFS cannot give absolute energy positions unless precise X-rays energy calibration was performed, that is not always the case. Therefore, from one report to the other the values may vary. Moreover, it is important to compare energy positions between hematite and titanates data recorded using the same experimental conditions, as in F.M.F. de Groot et al. [47]. In this report, likewise our data, the O 1s – Fe e_g and O 1s – Ti t_{2g} bands are clearly degenerate. Hereafter we interpret all energy positions relative to the O 1s – Fe t_{2g} one, of 529.9 eV, applying relative positions extracted from the literature.

Table 1: absolute and relative Fe and Ti peak positions in eV for the S1 sample, with respect to the Fe t_{2g} one (first column), extracted from the O K-edge NEXAFS spectra and compared to relevant data from literature. OSS position is identified at +2.2 eV from Fe t_{2g}. [†] expected position of the O 1s – Ti e_g considering +2.7 eV with respect to the O 1s – Fe t_{2g}.

Fe t_{2g} (eV)	Fe e_g / Ti t_{2g} (Δ) (eV)	OSS (Δ) (eV)	Ti e_g (Δ) (eV)	reference
529.9	531.3 (+1.4)	533.5 (+2.2)	534.0 (+2.7)[†]	this work
529.4	530.7 (+1.3)	-	533.3 (+2.6)	[47]
-	530.8	-	533.5 (+2.7)	[48]

Table 1 summarize the positions of the different hybridized Fe and Ti bands identified in the O K-edge NEXAFS. All resonances are presented also as relative spectral positions (Δ) to the O 1s – Fe t_{2g} at 529.9 eV. We report the peak positions extracted from Figure 4b in the first row. The 4th column gives the expected position for the O 1s – Ti e_g transition at Δ = +2.7 eV accordingly to reference [48]. Typically, the Fe d-orbital splitting in hematite is 1.4 eV, while the Ti d-orbital splitting for Ti^{4+} ion, likewise TiO_2, is 2.7 eV. The peak position we could assign to the O 1s – Ti e_g is at 533.5 eV, *i.e.* at a value Δ = +2.2 eV instead of the expected one at Δ = +2.7 eV. One could consider strong distortion effects of the octahedral symmetry, or a highly disordered surface [49], affecting the expected crystal field splitting. In this case, the dip at ~532 eV between the A and B spectral regions in Figure 4b, would be less pronounced, that is not the case in our spectra. Thus, the B peak in Figure 4b cannot be assigned to only the Ti e_g band and we address this peak as arising from the presence of OSS. These states, with highly oxidized character, offer to the electrolyte additional charge transfer possibilities, explaining the increased PEC activity [14]. Indeed, we probe the same states as the ones determined from the PEC measurements. During the PEC we directly access the contribution of these higher oxidation states (OSS) at the overall charge transfer reflected in the photocurrent measurement, while XAS probes them as available unoccupied levels by transition of core level electrons. It is interesting to mention here a recent report [25] where the authors studied induced oxygen vacancies upon additional thermal treatments

under N_2 atmosphere of their porous Ti-doped hematite photoanodes. Using XPS, they locate a contribution in the O 1s core level arising from oxygen vacancies at +2.4 eV binding energies compared to the contribution of the oxygen from the hematite lattice. It appears thus reasonable to consider this additional contribution from O 1s core level in the NEXAFS spectra and matching well the OSS spectral position. Consequently, we can reasonably assume that OSS are driven by the oxygen vacancies produced by the annealing under N_2.

As detailed elsewhere [14], we mention that we didn't find any Sn diffusion as often reported for the hematite based photoanodes deposited on FTO substrates (see for instance [50]). At the O K-edge (~533 eV) we would expect a characteristic spectral feature related to electronic transitions in the Sn 5p orbitals, that is missing from all our samples. As generally accepted, the Sn diffusion, if any, scales with the annealing temperature. Since both samples were prepared in the same temperature conditions (i.e. annealed at the same temperature 600 °C), if any Sn diffusion is present, should be of the same amount and therefore affect the PEC results at the same level. In addition, we tested the possible formation of nitride phases at the N K-edge (for Fe-N and/or Ti-N coordination). Nothing measurable could be measured thus at the N K-edge. We want to stress that, likewise the Sn diffusion, XAS loses its sensitivity for concentration values below ~0.1 %. While we cannot rule out definitively the formation of nitride phases, that would be certainly below the needed quantity to drive the reported enhancement upon N_2 annealing. On the other hand, we recall that the probability of obtaining nitrides by exposing an oxide in N_2 atmosphere, even at higher temperatures, is very low, being related to the high activation energy barrier of the N-N triple bond (940.95 kJ/mol) and most often the studies treating about metal nitrides synthesis report adopting alternative methods to the simple high temperature annealing (see for instance [51]).

2.3.2. Correlative measurements: STXM, spectro-ptychorahy and STEM

While S-XPEEM offers high surface selectivity, its spatial resolution is altered due to space charge effects [52], occurring especially in strongly 3D-shaped samples, like the ones measured here. Space charge effect arises from Coulomb collective repulsion of the photoelectrons generated in the surface region of our samples, resulting in a spatial broadening and therefore in resolution loss. To better resolve the spatial distribution associated with the spectral features discussed above, we measured the samples using STXM and spectro-ptychography. These are photon-in/photon-out techniques, exempted thus from space charge effects. In addition, the ptychography allows accessing increased resolution compared to conventional STXM, through ptychographic reconstruction of series of X-rays scattering images originating from overlapping regions on the sample [53,54]. This is, to the best of our knowledge, the first report of spectro-ptychography at Ti $L_{2,3}$ absorption edge, enabled by the use of a sCMOS camera equipped with an uncoated sensor providing high efficiency at low energies [55,56]. Further details about the ptychography implementation used here are given in the Methods section. All meaningful absorption edges (Ti $L_{2,3}$, N K, O K, Fe $L_{2,3}$) were first tested using standard STXM (i.e. using a photomultiplier tube detector) to identify best suited spectral features of interest on both S1 and S2 samples. It was possible thus to target where to perform spectro-ptychography measurements, a time-consuming approach both for acquisition and reconstruction. Thus, only the Ti $L_{2,3}$ edge obtained for the S1 sample (annealed under Nitrogen) appeared to be adapted for this correlative description that is discussed in the following, as one presenting outstanding spectral features probing directly the chemical and coordination nature of the pseudo-brookite surface region probed also by S-XPEEM. The 3D spectro-ptychography dataset ("spectro-PTYCHO_S1.gif") included in Supplementary Information exhibit additional spectral range across the O K-edge where we observe same OSS spectral position as in S-XPEEM (i.e. 533.5 eV).
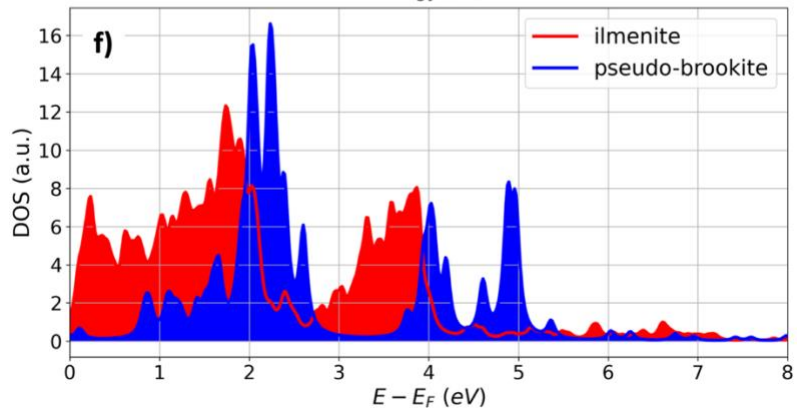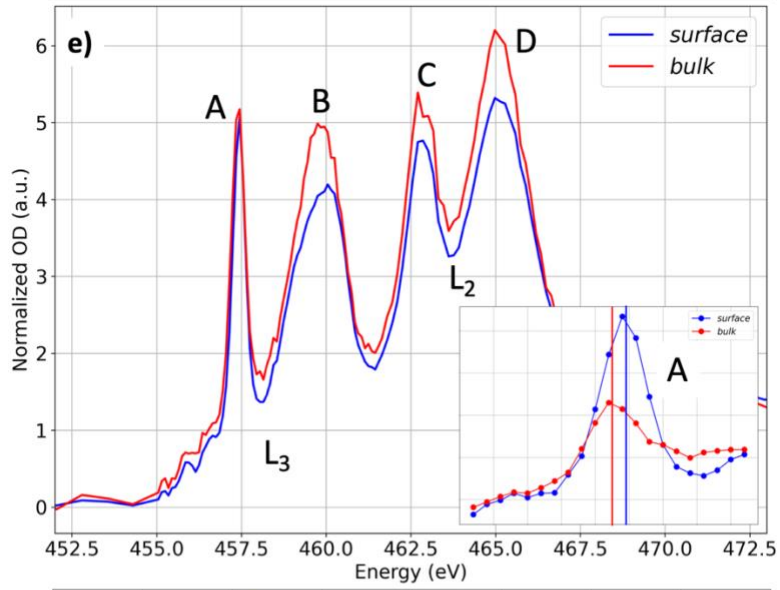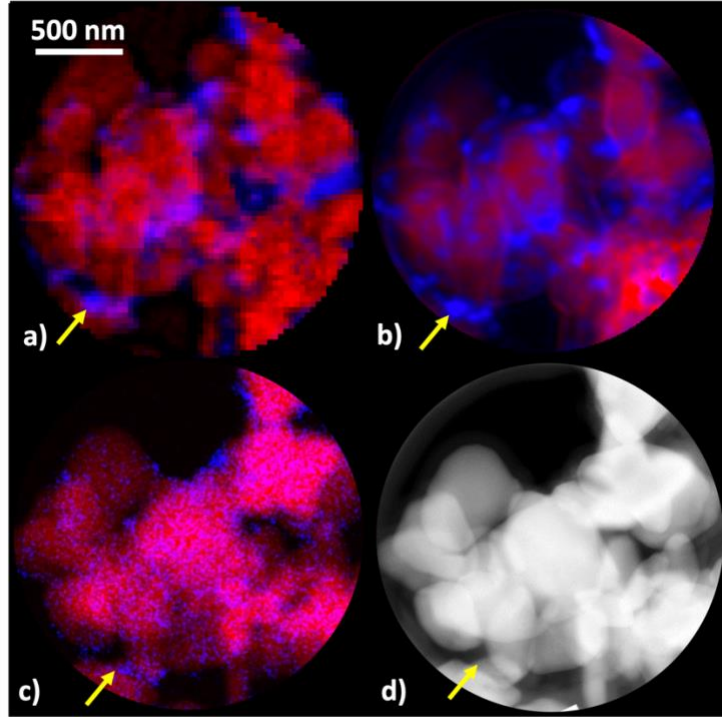
Figure 5. Overview of STXM, spectro-ptychography, and STEM (EDXS and HAADF) results obtained from the same N_2-annealed (S1) sample region, along with DFT calculations. Speciation maps obtained from STXM hyperspectral data (a), spectro-ptychography (b), elemental mapping from EDXS (c), and the corresponding HAADF image (d). Circular overlays were used in the images matching the support hole size (2 µm) to keep only the signal from the unsupported sample part (details in text and Supporting Information). The yellow arrows are guide to eyes pointing to the same particular sample position; e) Ti $L_{2,3}$ edge NEXAFS spectra of the surface Fe_2TiO_5 clusters (blue) and bulk Ti-doped hematite (red), used to obtain the speciation maps in a). The inset showing the spectral region (A) Ti L_3 t_{2g}, used for spectro-ptychography speciation map (b), exhibiting +0.1 eV energy shift for the surface component; f) summed t_{2g} and e_g bands calculated by DFT using model bulk structures for ilmenite (red) and pseudo-brookite (blue). Compared to ilmenite, pseudo-brookite exhibits energy shift toward higher binding energies, strongly increased t_{2g} and slightly reduced e_g integrated DOS.

Figure 5 presents overall results obtained using STXM, spectro-ptychography and STEM from the S1 sample. Rigorously the same sample location was measured using STXM (Figure 5a), spectro-ptychography (Figure 5b) and STEM in EDXS (Energy Dispersive X-ray Spectrometry) and HAADF (High Angle Annular Dark Field) modes (Figure 5 c and 5d, respectively), owing to the use of special hole-tagged SiN membranes (see Supporting Information – IV for details) which can be consecutively employed by different microscopy techniques. For better visualization, the yellow arrows point to the same particular sample position as guide to the eyes. Using STXM, we can afford describing the full NEXAFS spectral region covering Ti $L_{2,3}$ absorption edge, with high spectral resolution, in this case better than 0.1 eV. Indeed, hyperspectral data can be obtained with large number of spectral points while keeping a reasonable spatial resolution, adapting the scanning step-size at the used Fresnel zone plate, here 25 nm, giving a beam spot-size of 31 nm. In this manner we isolated two specific spectral components (Figure 5e), marked in blue and red and assigned for surface and bulk signals, respectively. The corresponding R(G)B color-coded map presented in Figure 5a was obtained using the SVD method implemented in the aXis2000 software after applying a drift correction to the recorded stack, similarly to the S-XPEEM images (Figure 3a and 3b). Here we choose to apply a circular overlay of 2 µm dimeter corresponding to the region exempted from the SiN support membrane contribution. Thus, the I_0 signal was taken from the free space around the nanoparticles and the corresponding signals, in OD terms, from the surface

clusters (blue) and bulk nanoparticles (red), were extracted correspondingly (Figure 5e). They compare well with those extracted from the S-XPEEM (Figure 4a): increased A:B branching ratio for the surface component of S1 sample. NEXAFS spectra extracted from the STXM exhibit two major additional spectral features. First, Ti L_3 t_{2g} peak corresponding to the surface clusters (blue) is shifted by +0.1 eV. Second, the same surface component in Figure 5e presents a strongly asymmetric B peak, that could not be evidenced using the S-XPEEM, because of the poorer spatial definition in that case. This asymmetry is in agreement with the pseudo-brookite character of the surface clusters [42], as suggested by S-XPEEM. The ilmenite-like overall spectral shape of the bulk component (red in Figure 5e) confirms substitutional Ti^{4+} inside the hematite structure [57]. Switching to spectro-ptychography is very handy at HERMES beamline, the standardly used 0D detector, a photomultiplier tube is replaced simply by a 2D detector, an sCMOS camera, without modifying the sample setup (for details see Methods section 4.4.3. and Supporting Information – IV). In this manner we could record spectro-ptychography data on the same region of interest (ROI) as the one used for STXM (Figure 5b). This R(G)B color-coded map was obtained measuring 21 energy points across the Ti L_3 t_{2g} (peak A in Figure 5e and inset) resonance, using SVD likewise for S-XPEEM and STXM. Compared to STXM, less spectral points are measured due mainly to the huge amount of generated data (*e.g.* more than 14 Go per X-rays energy point), difficult to analyze even using dedicated workstation equipped with multiple GPU (Graphics Processing Units). Within the ptychographic reconstructed image pixel size of 8.5 nm (Figure 5b), we can estimate surface clusters (blue) size spanning from ~10 nm to ~100 nm. It is important to mention here that STXM spectral components shown in Figure 5e were extracted as a second iteration during the cross analysis between STXM and spectro-ptychography data, the later allowing to better isolate a spatial region with pure "blue" component, associated to the surface clusters, used afterwards as input component for the SVD. Owing to NEXAFS strong chemical coordination

sensitivity we can spatially separate distinct spectral components. In other words, the chemical coordination allows reaching very good spatial resolution using spectro-ptychography (see also Figure S12). Compared to STXM, spectro-ptychography recovers both amplitude (absorption) and phase (dispersion) informations (Figure S12). Further analysis can be thus performed following the arguments used by Farmand et al. [58]. Such in-deep analysis of spectro-ptychography is however beyond the scope of this paper and will be treated elsewhere. An analytical STEM-EDX (Figure 5c) characterization performed on strictly the same area, confirms the presence of the Ti-rich area at the surface of the Ti-doped hematite particles. The HAADF image recorded simultaneously with the EDX one, is also shown (Figure 5d).

To confirm the origin of NEXAFS spectral characteristics at Ti $L_{2,3}$ absorption edge, *i.e.* +0.1 eV energy shift of the L_3 t_{2g} and the variation of A:B branching ratio, we performed DFT calculations on bulk structures from ilmenite, as model for Ti-doped hematite structure, and pseudo-brookite, following crystallographic structures shown in Figure S10. First, it is important to remind that NEXAFS probes unoccupied states via electronic transitions from core levels. DFT allows calculating the contribution to the density of states (DOS) of each orbital per atom of the unit cell. To compare with the NEXAFS experimental data, Figure 5f shows the summed contributions of the Ti 3d orbitals for ilmenite (red) and pseudo-brookite (blue), respectively. We remind here that the t_{2g} level (lower binding energy) is composed from d_{xy}, d_{xz} and d_{yz} orbitals, while e_g (higher binding energy) gathers the $d_{x^2-y^2}$ and d_{z^2} ones. All synchrotron X-rays measurements were performed using circular polarization such as to remove any contributions arising from charge anisotropies in the sample. Thus, assuming no particular orientation of the pseudo-brookite clusters, summing over all orbital orientation is valid for a simple comparison with the experimental data. Calculated DOS are in good agreement with those probed experimentally. First, pseudo-brookite

exhibits an energy shift toward higher energies. The calculated shift value (~ 1 eV) is much larger compared to the experimental measured value (0.1 eV). This is most probably related to the approximation made here, *i.e.* considering bulk pseudo-brookite structure and, most importantly, ilmenite structure to model the Ti-doped hematite. Indeed, the estimated Ti substitution level for our samples is less than 10 %, while ilmenite structure can be assimilated to 50 % Ti doping. Second, the experimental variation of the branching ratio A:B (Figure 5e) is perfectly reproduced in the calculated DOS. Thus, the pseudo-brookite presents increased A:B ratio compared to the ilmenite. In addition, the pseudo-brookite DOS presents two distinct features at +4 eV and +5 eV relative to the Femi level, that can be associated to the asymmetry of the e_g measured by NEXAFS (B peak in Figure 5e).

2.4. Crystallographic structure
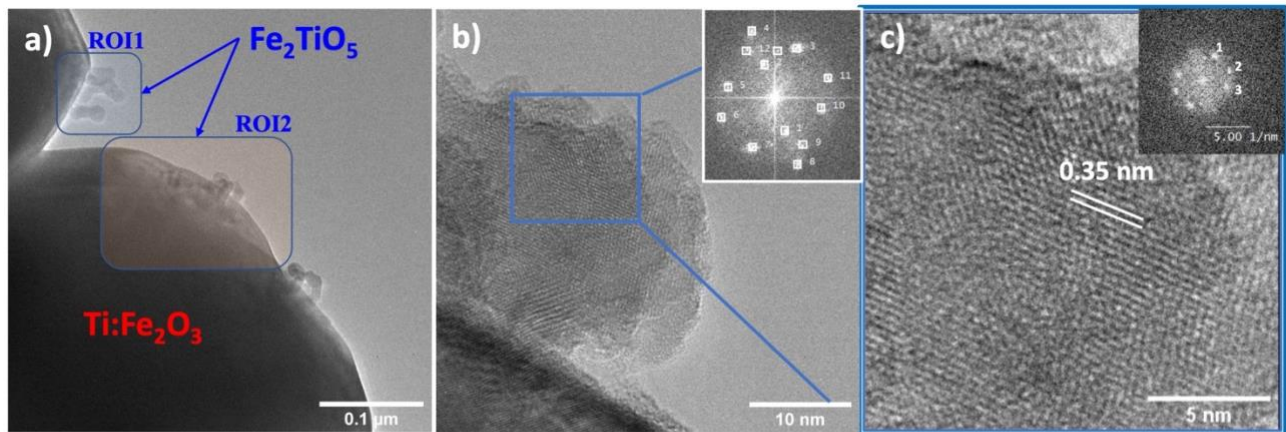
d) FFT of Ti50-hr_0013 (**S1**) -> **pseudo-brookite**

Plan	Spot#	d-Spacing (nm)	Rec. Pos.(1/nm)	Degrees to Spot 1	Degrees to x-axis	Amplitude
111	1	0.3342	2.992	176.81	-116.51	1018898.50
111	2	0.3277	3.052	0.00	66.68	1018898.50
101	3	0.3600	2.778	100.26	166.94	218105.34

Figure 6. STEM crystallographic measurements of S1 sample: a) nanoparticle detailed view exhibiting the surface clusters. Two distinct ROI are indicated presenting two types of morphology for the pseudo-brookite clusters; b) high resolution STEM cliché with associated FFT (Fast Fourier Transform) in the insets; c) cluster zoomed view showing well defined atomic planes with the associated FFT inset presenting bright diffraction spots corresponding to the pseudo-brookite structure; d) electron diffraction indexation with the 3 main spots arising from the pseudo-brookite structure.

Structural analysis performed by high resolution STEM (Figure 6) consolidates spectro-microscopy results about the nature of the surface clusters phase, namely the pseudo-brookite phase. Figure 6a shows the detail of a Ti-doped hematite nanoparticle presenting pseudo-brookite surface clusters. The size of these clusters, of few tens of nanometers, fits well the average size determined from spectro-ptychography. We observe two types of morphology for the pseudo-brookite clusters: one with pronounced 3D character (columnar-like) (Figure 6a – ROI1), with long chains composed of few clusters and where the interface between hematite nanoparticles and pseudo-brookite clusters is thus small (see also Figure S13). The second one, where shorter clusters chains are lying on a visible modified surface region of the hematite nanoparticles (Figure 6a – ROI2). Both morphologies can be recognized in Figure 5b obtained by spectro-ptychography, where we can clearly identify isolated "blue" spots along with elongated structures exhibiting pseudo-brookite spectral features. The similarity and complementarity between STEM and spectro-ptychography is further illustrated in Figure S14. Structural TEM investigation was performed using SAED (Selected Area Electron Diffraction). Figure 6b and 6c illustrate high resolution TEM images of a typical cluster isolated at the surface of the Ti-doped hematite nanoparticles. The diffractograms were obtained using FFT and used for structural indexation (Figure 6d). More details are given in Figure S13. We can identify spots arising from the hematite and pseudo-brookite structures, with their typical d-spacing at ~0.275 nm and ~0.355 nm, respectively.

We may attempt here an explanation for the mechanism of pseudo-brookite Fe_2TiO_5 formation, even though a proper structural *in situ* investigation was not conducted during this study. Let start our explanation following the arguments developed elsewhere [14], hypothesizing the existence of two kinds of Ti bonds in the bulk of the iron oxyhydroxide akaganeite structure formed after the ACG process: one substituting Fe in $Fe-O_6$ octahedra and the other linked with the Cl from the typical akaganeite tunnel structure. This assumption allows to explain the Ti segregation toward

the surface leading to Ti-rich phase upon annealing. Indeed, when increasing the temperature, the Chlorine bonded Ti will easily migrate toward the surface of the hematite nanorods leading to the observed surface segregation. Such segregation was reported equally for Ti-doped hematite obtained by different synthesis methods (see for instance [22]), but in the absence of adapted spectromicroscopy techniques like we report here, it was simply supposed that the Ti-rich phase is TiO$_2$. At the nanorod surface, the Ti-rich phase will present Ti-O$_6$ octahedra, but different (in terms of interatomic distances and angles of the octahedra) from those constituting the ilmenite like one (FeTiO$_3$), as supported by the Ti L$_{2,3}$ absorption spectral features (i.e. shift toward higher energies of the Ti L$_3$ t$_{2g}$ and asymmetry of the Ti L$_3$ e$_g$ peak). Indeed, the ilmenite can be assimilated with 50% substitutional Ti in Fe$_2$O$_3$, while Fe$_2$TiO$_5$ can be expressed as a phase aggregation: $Fe_2TiO_5 = Fe_2O_3 + TiO_2$. Interestingly, this phase aggregation process occurs only when annealing under Nitrogen, the air annealing producing only a Ti substitution gradient without TiO$_2$ nor pseudo-brookite phases formation in that case [14]. Most probably the presence of Oxygen stabilizes a homogeneous ilmenite-like phase at the surface of the Ti-doped hematite, while Nitrogen promotes phase separation between ilmenite-like ($Fe_{2-x}Ti_xO_3, with\ x \leq 1$) and pseudo-brookite.

3. Conclusions

In summary, we demonstrate enhanced photoelectrochemical performances using cheap and environment friendly hematite-based photoanodes, by simply adjusting the annealing step during the fabrication process, namely the use of Nitrogen atmosphere instead of the commonly used air one. To this purpose we present comparatively two samples: one annealed under Nitrogen and the other in air. Photocurrent measurements and impedance spectroscopy reveal that the main mechanism responsible for the enhanced activity is the increased charge transfer rate at interface with the electrolyte promoted by higher oxidation energy surface states. Combined S-XPEEM,

STXM and ptychography spectromicroscopies, employing state of the art instruments dedicated to synchrotron radiation characterisation, unravelled the origin of these surface states: formation of pseudo-brookite clusters at the surface of Ti-doped hematite nanorods. Using the specific XPEEM geometry we could access both surface and bulk chemical and coordination properties at nanoscale, evidencing modification in the O K-edge spectra arising from the formation of surface Ti-rich phase and the presence of oxygen vacancies promoting surface states in the probed unoccupied DOS. We report here for the first time, to the best of our knowledge, spectro-ptychography measurements at Ti $L_{2,3}$ absorption edges, demonstrating the very strong chemical coordination sensitivity of the approach, allowing to probe surface clusters as small as 10 nm. DFT calculations and complementary STEM measurements consolidated our findings about the formation of pseudo-brookite clusters at the surface of Ti-doped hematite nanoparticles, as the origin of the enhanced PEC activity. Finally, we demonstrate that low-tech approach allows escalating solar water splitting efficiency of photoanodes obtained from earth abundant material.

4. Methods

4.1 Samples preparation

Ti-substituted Fe_2O_3 nanorod photoanodes were grown on $F:SnO_2$ (FTO) substrates by a two-steps process. First, Ti-substituted akaganeite (Ti:β-FeOOH) films were elaborated by aqueous chemical growth (ACG) as detailed elsewhere [14]. Second, the akaganeite phase was converted in hematite by 600°C annealing in air or in a furnace quartz tube in the presence of N_2 flow (3 l/h). The annealing ramp is presented in Figure S15. The pH value of the growth solution was 1.4, the temperature during the growth was 95 °C and the deposition time was 24 h. These growth parameters allowed us to obtain carpet-like nanorods where the nanorods are perpendicular to the FTO substrate. Nanorods present 50 nm width and 200 nm length average values. Following this

procedure we obtained a Ti substitution level, on average, of 9%, following an increasing gradient from the FTO substrate toward the top part of the layer [14]. For XPEEM and STXM spectromicroscopies samples were prepared collecting Ti-doped iron oxyhydroxide (FeOOH) powder from the flasks used for the ACG process and left several days at room temperature for dehydration. The FeOOH powder was then annealed at 600°C either in air or under N_2 controlled flow conditions to obtain the hematite phase. Hematite powder was drop-casted using a solvent carrier obtained from 1:1 isopropanol in ultra-pure water, either on gold-plated Si wafers for S-XPEEM or on location-tagged holey TEM SiN membranes, for STXM (and spectro-ptychography) and STEM measurements. It is important mentioning here that no signs of surface sample alteration were observed due to the use of isopropanol – water mixture carrier. Such alterations would have hindered especially the data recorded in XPEEM, strongly sensitive to the surface topmost atomic layers. In addition, the PEC results are fully coherent with the XPEEM ones.

4.2. Photocurrent measurement

Stabilized values of the photocurrent were measured using a dedicated setup equipped with an UV-vis light source (Newport 1000 W Xe arc lamp), a three-electrode cell allowing front illumination of the photoanode and a Princeton Applied Research 263A potentiostat. All measurements were performed at room temperature using 0.1 M NaOH as electrolyte the samples are mounted as working electrode, a platinum wire is used as counter electrode, and an Ag/AgCl electrode as reference.

4.3. Electrochemical impedance spectroscopy (EIS) measurements

A CompactStat IVIUM potentiostat connected to a three-electrode photoelectrochemical H-cell (Redox.me), where hematite samples are mounted as working electrode, allowed us to measure cell impedance, Z, as a function of the frequency in the 10 Hz – 900 kHz range and of the applied potential varying between 0.7 – 1.6 V *vs.* RHE. The complex impedance:

$$Z = \frac{V(\omega)}{I(\omega)} = Z_{re} + jZ_{img}$$

contains informations on the RC-like equivalent circuit corresponding to the photoanode-electrolyte interface. These measurements allowed us to obtain Nyquist plots: $|Z_{img}|$ *vs.* (Z_{re}, f) and from the modeling of these data using IVIUM software applied on the equivalent RC circuit presented in Figure S3, we obtained Mott-Schottky plots and estimated flat band potential and carrier concentration (see Supporting Information for more details).

4.4. X-rays spectromicroscopy

Spectromicroscopy combines milli-eV spectral and nanometer spatial resolutions allowing to address therefore nanoscale physical and chemical properties. All data presented hereafter were obtained using the two microscopes available at the HERMES beamline [59] from the French SOLEIL synchrotron facility. Combining these techniques is of a particular interest when seeking surface/bulk information with very good spectral and spatial resolutions. Differentiation in spatial regions is gained through NEXAFS (Near Edge X-ray Absorption Fine Structure) contrast mechanism.

4.4.1. Shadow X-ray Photo-Emission Electron Microscopy (S-XPEEM)

We employed XPEEM [60] to locally probe the surface chemistry and the electronic structure of the samples. XPEEM is surface selective and uses the well-known photoelectric effect (Einstein, Nobel Prize 1921) as main contrast mechanism. It is known that, due to the very short electron mean free path, λ_e, XPEEM, likewise XPS, is "blind" for photoelectrons generated deeper than ~3 nm ($3 \cdot \lambda_e$) from the surface [61]. Nevertheless, the specific XPEEM apparatus geometry, namely the 16° incidence angle of the X-rays with respect to the sample surface plane, allow accessing equally bulk information, gathered from the sample shadow projected by the X-rays on the supporting substrate. A detailed schematic is given in Figure S7. Pioneered by Kimling et al. [62],

the shadow X-rays photo-emission electron microscopy (S-XPEEM) was employed to unravel complex buried magnetic structures.

4.4.2. Scanning Transmission X-rays Microscopy (STXM)

STXM is well established technique [63] exploiting the X-rays absorption as main contrast mechanism, in a raster scheme where each pixel value obeys the Beer-Lambert law, $I = I_0 \cdot e^{-\mu(E) \cdot \rho \cdot d}$, with I the transmitted intensity, I_0 the direct X-ray beam intensity, $\mu(E)$ the energy dependent mass attenuation coefficient, ρ the mass density, and d the thickness of the sample. It is thus convenient to quantify the sample's material parameters through the optical density (OD), measured as $\log(I_0/I)$. In addition, the $\mu(E)$ is accessed recording hyperspectral data (energy stacks), where the energy of the impinging X-rays is tuned, and an image is recorded at each energy point. One can thus define speciation maps where each spatially resolved pixel carry well defined spectral information.

4.4.3. Spectro-ptychography

The spectro-ptychography is performed at HERMES beamline at SOLEIL synchrotron, replacing the standardly used photomultiplier tube (PMT) with an sCMOS camera [55]. For each X-rays energy point, scattering images are recorded at each (X,Y) sample coordinate and the final real space image per energy point is obtained using the ptychographic reconstruction algorithm implemented in the PyNX suite [64]. Amplitude and phase reconstructed images are reassembled in stacks and treated as STXM energy stacks, *i.e.* drift correction and SVD. The acquisition control is ensured using Python through the PyTango binding allowing to interact with the sCMOS camera Tango device. An external clock gating scheme is used to trigger the camera, such as to obtain the synchronization between the sample stage positioning and the camera exposure. Two timing schemes are employed: fast one, typically at 20 fps, and a slow one, typically at 10 or 5 fps. The fast scheme is used simply to replace the normal PMT, STXM images being reconstructed in real

time integrating the bright field of the images. This is used for alignment, sample navigation and focusing, likewise in standard STXM experiments. The slow scheme is used when recording data for PyNX ptychographic reconstructions. For the data presented in this paper we used generally 2.5×2.5 µm^2 scanning sample areas and a defocused 1 µm X-ray beam spot size.

4.5. Transmission electron microscopy

The electron microscopy analyses were performed on a JEOL 2100 FEG S/TEM microscope operating at 200 kV and equipped with a probe spherical aberration corrector. For the acquisition of HAADF images in the STEM mode, a spot size of 0.13 nm, a current density of 140 pA, a camera focal length of 8 cm, which corresponds to inner and outer diameters of the annular detector of 73 and 194 mrad, have been used. The elemental maps were also recorded in the STEM mode by EDXS using a silicon drift detector (SDD) with a sensor size of 60 mm^2.

4.6. Density Functional Theory calculations

Electronic structure calculations of ilmenite and pseudo-brookite phases have been performed using the very efficient localized-orbital basis set DFT code Fireball [65,66]. In this method, the self-consistency is achieved over the occupation numbers through the Harris functional [67] and LDA exchange-correlation energy is calculated using the efficient multi-center weighted exchange correlation density approximation (McWEDA) [68]. This method has already been used for the study of molecular adsorption on Fe_3O_4 surfaces in good agreement with experimental determination [69].

Supporting Information

CRediT authorship contribution statement

Conceptualization, S. Stanescu and D. Stanescu; data curation, S. Stanescu, D. Stanescu, T. Alun, D. Ihiawakrim and Y. J. Dappe; formal analysis, S. Stanescu, D. Stanescu, D. Ihiawakrim, O. Ersen and Y. J. Dappe; funding acquisition, S. Stanescu and D. Stanescu; investigation, S. Stanescu, T. Alun, D. Ihiawakrim and D. Stanescu; methodology, S. Stanescu and D. Stanescu; project administration, S. Stanescu and D. Stanescu; spectro-ptychography acquisition software, S. Stanescu; supervision, S. Stanescu; validation, S. Stanescu, D. Stanescu, Y. J . Dappe and O. Ersen; writing – original draft, S. Stanescu and D. Stanescu; and writing – review & editing, all.

References

[1]   R. Van De Krol, M. Gratzel, Photoelectrochemical hydrogen production using visible light, Springer, 2012. https://doi.org/10.1007/978-1-4614-1380-6.

[2]   H.C. Nguyën, F.A. Garcés-Pineda, M. De Fez-Febré, J.R. Galán-Mascarós, N. López, Non-redox doping boosts oxygen evolution electrocatalysis on hematite, Chem. Sci. 11 (2020) 2464–2471. https://doi.org/10.1039/c9sc05669f .

[3]   X. Zhang, C. Cao, A. Bieberle-Hütter, Orientation sensitivity of oxygen evolution reaction on hematite, J. Phys. Chem. C. 120 (2016) 28694–28700. https://doi.org/10.1021/acs.jpcc.6b10553 .

[4]   E. Fabbri, A. Habereder, K. Waltar, R. Kötz, T.J. Schmidt, Developments and perspectives of oxide-based catalysts for the oxygen evolution reaction, Catal. Sci. Technol. 4 (2014) 3800–3821. https://doi.org/10.1039/c4cy00669k .

[5]   B. Klahr, S. Gimenez, F. Fabregat-Santiago, T. Hamann, J. Bisquert, Water oxidation at hematite photoelectrodes: The role of surface states, J. Am. Chem. Soc. 134 (2012) 4294–4302. https://doi.org/10.1021/ja210755h .

[6]   M. Rioult, H. Magnan, D. Stanescu, A. Barbier, Single crystalline hematite films for solar water splitting: Ti-doping and thickness effects, J. Phys. Chem. C. 118 (2014) 3007–3014. https://doi.org/10.1021/jp500290j .

[7]   B. Zhao, T.C. Kaspar, T.C. Droubay, J. McCloy, M.E. Bowden, V. Shutthanandan, S.M. Heald, S.A. Chambers, Electrical transport properties of Ti-doped Fe 2O 3(0001) epitaxial films, Phys. Rev. B - Condens. Matter Mater. Phys. 84 (2011) 1–9. https://doi.org/10.1103/PhysRevB.84.245325 .

[8]   T.P. Ruoko, A. Hiltunen, T. Iivonen, R. Ulkuniemi, K. Lahtonen, H. Ali-Löytty, K. Mizohata, M. Valden, M. Leskelä, N. V. Tkachenko, Charge carrier dynamics in tantalum oxide overlayered and tantalum doped hematite photoanodes, J. Mater. Chem. A. 7 (2019) 3206–3215. https://doi.org/10.1039/C8TA09501A .

[9]   M. Rioult, R. Belkhou, H. Magnan, D. Stanescu, S. Stanescu, F. Maccherozzi, C. Rountree, A. Barbier, Local electronic structure and photoelectrochemical activity of partial chemically etched Ti-doped hematite, Surf. Sci. 641 (2015) 310. https://doi.org/10.1016/j.susc.2015.01.002 .

[10]   X. Wang, K.Q. Peng, Y. Hu, F.Q. Zhang, B. Hu, L. Li, M. Wang, X.M. Meng, S.T. Lee, Silicon/hematite core/shell nanowire array decorated with gold nanoparticles for unbiased solar water oxidation, Nano Lett. 14 (2014) 18–23. https://doi.org/10.1021/nl402205f .

[11]   H. Jun, B. Im, J.Y. Kim, Y.O. Im, J.W. Jang, E.S. Kim, J.Y. Kim, H.J. Kang, S.J. Hong, J.S. Lee, Photoelectrochemical water splitting over ordered honeycomb hematite electrodes stabilized by alumina shielding, Energy Environ. Sci. 5 (2012) 6375–6382. https://doi.org/10.1039/c1ee02526k .

[12]   C. Yang, W. Wei, Y. Gong, L. Yan, K. Zhao, J. Zhou, J. Feng, A. Zhang, M. Qin, M. Zeng, Z. Fan, X. Gao, G. Zhou, X. Lu, J.M. Liu, Effect of substrate and intermediate layer on the conductivity and charge transport properties of epitaxial BaTiO3-δ films, J. Phys.

D. Appl. Phys. 50 (2017). https://doi.org/10.1088/1361-6463/aa98ad .

[13]   H.R. Devi, B.C. Ong, X. Zhao, Z. Dong, K.K. Nanda, Z. Chen, Insights into Improving Photoelectrochemical Water-Splitting Performance Using Hematite Anode, Energy Technol. 2100457 (2021). https://doi.org/10.1002/ente.202100457 .

[14]   D. Stanescu, M. Piriyev, V. Villard, C. Mocuta, A. Besson, D. Ihiawakrim, O. Ersen, J. Leroy, S.G. Chiuzbaian, A.P. Hitchcock, S. Stanescu, Characterizing surface states in hematite nanorod photoanodes, both beneficial and detrimental to solar water splitting efficiency, J. Mater. Chem. A. 8 (2020) 20513–20530. https://doi.org/10.1039/d0ta06524b .

[15]   M. Rioult, D. Stanescu, E. Fonda, A. Barbier, H. Magnan, Oxygen Vacancies Engineering of Iron Oxides Films for Solar Water Splitting, J. Phys. Chem. C. 120 (2016) 7482–7490. https://doi.org/10.1021/acs.jpcc.6b00552 .

[16]   S. Seenivasan, S. Adhikari, D.H. Kim, Surface restructuring of hematite photoanodes through ultrathin NiFeOx Catalyst: Amplified charge collection for solar water splitting and pollutant degradation, Chem. Eng. J. 422 (2021) 130137. https://doi.org/10.1016/j.cej.2021.130137 .

[17]   D.K. Zhong, M. Cornuz, K. Sivula, M. Grätzel, D.R. Gamelin, Photo-assisted electrodeposition of cobalt-phosphate (Co-Pi) catalyst on hematite photoanodes for solar water oxidation, Energy Environ. Sci. 4 (2011) 1759–1764. https://doi.org/10.1039/c1ee01034d .

[18]   P.Y. Tang, L.J. Han, F.S. Hegner, P. Paciok, M. Biset-Peiró, H.C. Du, X.K. Wei, L. Jin, H.B. Xie, Q. Shi, T. Andreu, M. Lira-Cantú, M. Heggen, R.E. Dunin-Borkowski, N. López, J.R. Galán-Mascarós, J.R. Morante, J. Arbiol, Boosting Photoelectrochemical Water Oxidation of Hematite in Acidic Electrolytes by Surface State Modification, Adv. Energy Mater. 9 (2019) 1–11. https://doi.org/10.1002/aenm.201901836 .

[19]   J.M. Gardner, S. Kim, P.C. Searson, G.J. Meyer, Electrodeposition of nanometer-sized ferric oxide materials in colloidal templates for conversion of light to chemical energy, J. Nanomater. 2011 (2011). https://doi.org/10.1155/2011/737812 .

[20]   J.Y. Kim, J.W. Jang, D.H. Youn, G. Magesh, J.S. Lee, A stable and efficient hematite photoanode in a neutral electrolyte for solar water splitting: Towards stability engineering, Adv. Energy Mater. 4 (2014) 1–7. https://doi.org/10.1002/aenm.201400476 .

[21]   I.S. Cho, H.S. Han, M. Logar, J. Park, X. Zheng, Enhancing Low-Bias Performance of Hematite Photoanodes for Solar Water Splitting by Simultaneous Reduction of Bulk, Interface, and Surface Recombination Pathways, Adv. Energy Mater. 6 (2016) 1–9. https://doi.org/10.1002/aenm.201501840 .

[22]   Z. Zhang, I. Karimata, H. Nagashima, S. Muto, K. Ohara, K. Sugimoto, T. Tachikawa, Interfacial oxygen vacancies yielding long-lived holes in hematite mesocrystal-based photoanodes, Nat. Commun. 10 (2019) 4832. https://doi.org/10.1038/s41467-019-12581-z .

[23]   X. Zhao, J. Feng, S. Chen, Y. Huang, T.C. Sum, Z. Chen, New insight into the roles of oxygen vacancies in hematite for solar water splitting, Phys. Chem. Chem. Phys. 19 (2017) 1074–1082. https://doi.org/10.1039/c6cp06410h .

[24] P. Biswas, A. Ainabayev, A. Zhussupbekova, F. Jose, R. O'Connor, A. Kaisha, B. Walls, I. V. Shvets, Tuning of oxygen vacancy-induced electrical conductivity in Ti-doped hematite films and its impact on photoelectrochemical water splitting, Sci. Rep. 10 (2020) 2–10. https://doi.org/10.1038/s41598-020-64231-w .

[25] Z. Wang, X. Mao, P. Chen, M. Xiao, S.A. Monny, S. Wang, M. Konarova, A. Du, L. Wang, Understanding the Roles of Oxygen Vacancies in Hematite-Based Photoelectrochemical Processes, Angew. Chemie - Int. Ed. 58 (2019) 1030–1034. https://doi.org/10.1002/anie.201810583.

[26] A. Pu, J. Deng, M. Li, J. Gao, H. Zhang, Y. Hao, J. Zhong, X. Sun, Coupling Ti-doping and oxygen vacancies in hematite nanostructures for solar water oxidation with high efficiency, J. Mater. Chem. A. 2 (2014) 2491–2497. https://doi.org/10.1039/c3ta14575a.

[27] S. Berardi, J. Kopula Kesavan, L. Amidani, E.M. Meloni, M. Marelli, F. Boscherini, S. Caramori, L. Pasquini, Better Together: Ilmenite/Hematite Junctions for Photoelectrochemical Water Oxidation, ACS Appl. Mater. Interfaces. 12 (2020) 47435–47446. https://doi.org/10.1021/acsami.0c12275 .

[28] J. Deng, X. Lv, J. Liu, H. Zhang, N. Kaiqi, H. Caihao, W. Jiaou, X. Sun, J. Zhong, S.T. Lee, Thin-Layer Fe2TiO5 on Hematite for Efficient Solar Water Oxidation, ACS Nano. 9 (2015) 5348–5356. https://doi.org/10.1021/acsnano.5b01028 .

[29] P.S. Bassi, R.P. Antony, P.P. Boix, Y. Fang, J. Barber, L.H. Wong, Crystalline Fe2O3/Fe2TiO5 heterojunction nanorods with efficient charge separation and hole injection as photoanode for solar water oxidation, Nano Energy. 22 (2016) 310–318. https://doi.org/10.1016/j.nanoen.2016.02.013 .

[30] X. Lv, K. Nie, H. Lan, X. Li, Y. Li, X. Sun, J. Zhong, S.T. Lee, Fe2TiO5-incorporated hematite with surface P-modification for high-efficiency solar water splitting, Nano Energy. 32 (2017) 526–532. https://doi.org/10.1016/j.nanoen.2017.01.001 .

[31] A. Hankin, F.E. Bedoya-Lora, J.C. Alexander, A. Regoutz, G.H. Kelsall, Flat band potential determination: Avoiding the pitfalls, J. Mater. Chem. A. 7 (2019) 26162–26176. https://doi.org/10.1039/c9ta09569a .

[32] K. Sivula, Mott−Schottky Analysis of Photoelectrodes: Sanity Checks Are Needed, ACS Energy Lett. 6 (2021) 2549−2551. https://doi.org/10.1021/acsenergylett.1c01245 .

[33] R. Jiang, C. Chen, S. Zheng, The non-linear fitting method to analyze the measured M-S plots of bipolar passive films, Electrochim. Acta. 55 (2010) 2498–2504. https://doi.org/10.1016/j.electacta.2009.11.093 .

[34] S. Gao, C. Dong, H. Luo, K. Xiao, X. Li, Electrochemical Behavior and Nonlinear Mott-Schottky Characterization of a Stainless Steel Passive Film, Anal. Lett. 47 (2014) 1162–1181. https://doi.org/10.1080/00032719.2013.865201 .

[35] E.J. Lee, S. Il Pyun, Analysis of nonlinear Mott-Schottky plots obtained from anodically passivating amorphous and polycrystalline TiO2 films, J. Appl. Electrochem. 22 (1992) 156–160. https://doi.org/10.1007/BF01023817.

[36] V. Archana, J. Joseph Prince, S. Kalainathan, Simple One-Step Leaf Extract-Assisted Preparation of α -Fe2O3Nanoparticles, Physicochemical Properties, and Its Sunlight-

Driven Photocatalytic Activity on Methylene Blue Dye Degradation, J. Nanomater. 2021 (2021). https://doi.org/10.1155/2021/8570351.

[37]   X.G. Zhang, Electrochemistry of Silicon and Its Oxide, Springer, Boston, MA, 2001. https://doi.org/10.1007/b100331

[38]   S. Tengeler, Cubic Silicon Carbide For Direct Photoelectrochemical Water Splitting, Grenoble Alpes University, France, 2018. https://tel.archives-ouvertes.fr/tel-01718565 .

[39]   R. Liu, C. Stephani, J.J. Han, K.L. Tan, D. Wang, Silicon nanowires show improved performance as photocathode for catalyzed carbon dioxide photofixation, Angew. Chemie - Int. Ed. 52 (2013) 4225–4228. https://doi.org/10.1002/anie.201210228.

[40]   J. Li, W. Wan, C.A. Triana, H. Chen, Y. Zhao, C.K. Mavrokefalos, G.R. Patzke, Reaction kinetics and interplay of two different surface states on hematite photoanodes for water oxidation, Nat Commun. 12 (2021) 255. https://doi.org/10.1038/s41467-020-20510-8.

[41]   http://unicorn.mcmaster.ca/aXis2000.html.

[42]   F.M.F. de Groot, M.O. Figueiredo, M.J. Basto, M. Abbate, H. Petersen, J.C. Fuggle, 2 p X-ray absorption of titanium in minerals, Phys. Chem. Miner. 19 (1992) 140–147. https://doi.org/10.1007/BF00202101.

[43]   J.P. Crocombette, F. Jollet, Ti 2p x-ray absorption in titanium dioxides (TiO2): The influence of the cation site environment, Am. Lab. 26 (1994) 10811–10821. https://iopscience.iop.org/article/10.1088/0953-8984/6/49/022 .

[44]   B.P. Von Der Heyden, A.N. Roychoudhury, T. Tyliszczak, S.C.B. Myneni, Investigating nanoscale mineral compositions: Iron L3-edge spectroscopic evaluation of iron oxide and oxy-hydroxide coordination, Am. Mineral. 102 (2017) 674–685. https://doi.org/10.2138/am-2017-5805.

[45]   W.Q. Guo, S. Malus, D.H. Ryan, Z. Altounian, Crystal structure and cation distributions in the FeTi2O5-Fe2TiO5 solid solution series, J. Phys. Condens. Matter. 11 (1999) 6337–6346. https://doi.org/10.1088/0953-8984/11/33/304.

[46]   F. Frati, M.O.J.Y. Hunault, F.M.F. De Groot, Oxygen K - edge X - ray Absorption Spectra, Chem. Rev. 120 (2020) 4056–4110. https://doi.org/10.1021/acs.chemrev.9b00439.

[47]   F.M.F. de Groot, M. Grioni, J.C. Fuggle, Oxygen 1s x-ray-absorption edges of transition-metal oxides, Phys. Rev. B. 40 (1989) 5715–5723. https://doi.org/10.1103/PhysRevB.40.5715 .

[48]   C.X. Kronawitter, M. Kapilashrami, J.R. Bakke, S.F. Bent, C.H. Chuang, W.F. Pong, J. Guo, L. Vayssieres, S.S. Mao, TiO 2-SnO 2:F interfacial electronic structure investigated by soft x-ray absorption spectroscopy, Phys. Rev. B. 85 (2012) 125109. https://doi.org/10.1103/PhysRevB.85.125109.

[49]   L. Soriano, M. Abbate, J. Vogel, J.C. Fuggle, A. Fernández, A.R. González-Elipe, M. Sacchi, J.M. Sanz, Chemical changes induced by sputtering in TiO2 and some selected titanates as observed by X-ray absorption spectroscopy, Surf. Sci. 290 (1993) 427–435. https://doi.org/10.1016/0039-6028(93)90725-Y.

[50]   J. Park, K.-Y. Yoon, T. Kim, H. Jang, M.-J. Kwak, J. Y. Kim, J.-H. Jang, A highly

transparent thin film hematite with multi-element dopability for an efficient unassisted water splitting system, Nano Energy 76 (2020) 105089. https://doi.org/10.1016/j.nanoen.2020.105089.

[51] Q. Luo, C. Lu, L. Liu, M. Zhu, A review on the synthesis of transition metal nitride nanostructures and their energy related applications, Green Energy & Environment (2022) https://doi.org/10.1016/j.gee.2022.07.002.

[52] D. Wilson, C. Schmitz, D. Rudolf, C. Wiemann, C.M. Schneider, L. Juschkin, On space charge effects in laboratory-based photoemission electron microscopy using compact gas discharge extreme ultraviolet sources, New J. Phys. 22 (2020) 103019. https://doi.org/10.1088/1367-2630/abbc29.

[53] F. Pfeiffer, X-ray ptychography, Nat. Photonics. 12 (2018) 9–17. https://doi.org/10.1038/s41566-017-0072-5.

[54] D.A. Shapiro, S. Babin, R.S. Celestre, W. Chao, R.P. Conley, P. Denes, B. Enders, P. Enfedaque, S. James, J.M. Joseph, H. Krishnan, S. Marchesini, K. Muriki, K. Nowrouzi, S.R. Oh, H. Padmore, T. Warwick, L. Yang, V. V. Yashchuk, Y.S. Yu, J. Zhao, An ultrahigh-resolution soft x-ray microscope for quantitative analysis of chemically heterogeneous nanomaterials, Sci. Adv. 6 : eabc49 (2020) 1–8. https://doi.org/10.1126/sciadv.abc4904.

[55] K. Desjardins, K. Medjoubi, M. Sacchi, H. Popescu, R. Gaudemer, R. Belkhou, S. Stanescu, S. Swaraj, A. Besson, J. Vijayakumar, S. Pautard, A. Noureddine, P. Mercere, P. Da Silva, F. Orsini, C. Menneglier, N. Jaouen, Backside-illuminated scientific CMOS detector for soft X-ray resonant scattering and ptychography, J. Synchrotron Radiat. 27 (2020) 1577–1589. https://doi.org/10.1107/S160057752001262X .

[56] N. Mille, H. Yuan, J. Vijayakumar, S. Stanescu, S. Swaraj, K. Desjardins, V. Favre-Nicolin, R. Belkhou, A.P. Hitchcock, Ptychography at the carbon K-edge, Commun. Mater. 3 (2022) 1–8. https://doi.org/10.1038/s43246-022-00232-8.

[57] F.M.F. de Groot, L2,3 x-ray-absorption edges of d0 compounds: K+, Ca2+, Sc3+, and Ti4+ in Oh (octahedral) symmetry, Phys. Rev. B. 41 (1990) 928. https://doi.org/10.1103/PhysRevB.41.928.

[58] M. Farmand, R. Celestre, P. Denes, A.L.D. Kilcoyne, S. Marchesini, H. Padmore, T. Tyliszczak, T. Warwick, X. Shi, J. Lee, Y.S. Yu, J. Cabana, J. Joseph, H. Krishnan, T. Perciano, F.R.N.C. Maia, D.A. Shapiro, Near-edge X-ray refraction fine structure microscopy, Appl. Phys. Lett. 110 (2017) 063101. https://doi.org/10.1063/1.4975377.

[59] R. Belkhou, S. Stanescu, S. Swaraj, A. Besson, M. Ledoux, M. Hajlaoui, D. Dalle, HERMES: a soft X-ray beamline dedicated to X-ray microscopy, J. Synchrotron Radiat. 22 (2015) 968–979. https://doi.org/10.1107/S1600577515007778.

[60] E. Bauer, Surface microscopy with low energy electrons, Springer, 2014. https://doi.org/10.1007/978-1-4939-0935-3.

[61] P. Deimel, F. Allegretti, ELECTRON SPECTROSCOPY OF SURFACES Elemental and Chemical Analysis with X-ray Photoelectron Spectroscopy, 2016. https://www.ph.tum.de/academics/org/labs/fopra/docs/userguide-35.en.pdf.

[62] J. Kimling, F. Kronast, S. Martens, T. Böhnert, M. Martens, J. Herrero-Albillos, L. Tati-Bismaths, U. Merkt, K. Nielsch, G. Meier, Photoemission electron microscopy of three-dimensional magnetization configurations in core-shell nanostructures, Phys. Rev. B. 84, (2011) 174406. https://doi.org/10.1103/PhysRevB.84.174406.

[63] A.P. Hitchcock, "Soft x-ray imaging and spectromicroscopy," in: G. Van Tendeloo, D. Van Dyck, S.J. Pennycook (Eds.), Vol. II Handb. Nanoscopy, Chap.22, 2012.

[64] V. Favre-Nicolin, G. Girard, S. Leake, J. Carnis, Y. Chushkin, J. Kieffer, P. Paleo, M.I. Richard, PyNX: High-performance computing toolkit for coherent X-ray imaging based on operators, J. Appl. Crystallogr. 53 (2020) 1404–1413. https://doi.org/10.1107/S1600576720010985.

[65] J.P. Lewis, P. Jelínek, J. Ortega, A.A. Demkov, D.G. Trabada, B. Haycock, H. Wang, G. Adams, J.K. Tomfohr, E. Abad, H. Wang, D.A. Drabold, Advances and applications in the FIREBALL ab initio tight-binding molecular-dynamics formalism, Phys. Status Solidi Basic Res. 248 (2011) 1989–2007. https://doi.org/10.1002/pssb.201147259.

[66] M.A. Basanta, Y.J. Dappe, P. Jelínek, J. Ortega, Optimized atomic-like orbitals for first-principles tight-binding molecular dynamics, Comput. Mater. Sci. 39 (2007) 759–766. https://doi.org/10.1016/j.commatsci.2006.09.003.

[67] J. Harris, Simplified method for calculating the energy of weakly interacting fragments, Phys. Rev. B. 31 (1985) 1770–1779. https://doi.org/10.1103/PhysRevB.31.1770.

[68] P. Jelínek, H. Wang, J.P. Lewis, O.F. Sankey, J. Ortega, Multicenter approach to the exchange-correlation interactions in ab initio tight-binding methods, Phys. Rev. B - Condens. Matter Mater. Phys. 71 (2005) 1–9. https://doi.org/10.1103/PhysRevB.71.235101.

[69] V.E. Campbell, M. Tonelli, I. Cimatti, J.B. Moussy, L. Tortech, Y.J. Dappe, E. Rivière, R. Guillot, S. Delprat, R. Mattana, P. Seneor, P. Ohresser, F. Choueikani, E. Otero, F. Koprowiak, V.G. Chilkuri, N. Suaud, N. Guihéry, A. Galtayries, F. Miserque, M.A. Arrio, P. Sainctavit, T. Mallah, Engineering the magnetic coupling and anisotropy at the molecule-magnetic surface interface in molecular spintronic devices, Nat. Commun. 7 (2016) 13646. https://doi.org/10.1038/ncomms13646.